

ARTICLE TYPE

Computational modeling of uniaxial antiferroelectric and antiferroelectric-like actuator

Binh H. Nguyen | Véronique Rochus

¹Department of Sensor and Actuator Technologies,
imec, 3001 Leuven, Belgium**Correspondence**Corresponding author: Binh H. Nguyen
Email: binh.nguyen@imec.be**Abstract**

Recently, antiferroelectric and antiferroelectric-like materials have regained interest for electronic devices, such as field-effect transistors, memory, and transducers. Particularly, in micro/nano-electromechanical coupling systems, such as actuators, these innovative materials, with their peculiar phase transition between antiferroelectric and ferroelectric phases, show promise in offering large electro-strain, fast response, and low power consumption devices. However, compared to the numerous computational models of ferroelectric actuators, numerical modeling of antiferroelectric and antiferroelectric-like actuators remains relatively unexplored. In this paper, we propose a phenomenological model of a uni-axial antiferroelectric and antiferroelectric-like actuators based on their switching polarization behavior. Specifically, both the double hysteresis loop of antiferroelectric materials and the pinched hysteresis loop of antiferroelectric-like materials can be captured by two hyperbolic tangent functions. This allows us to cast a polarization-dependent strain and piezoelectric tensor into the constitutive laws. The proposed model is then implemented into a finite element framework, in which the voltage-induced deformation can be solved using the Newton-Raphson procedure. Numerical examples of both antiferroelectric and antiferroelectric-like actuators are illustrated and compared with experimental data, showing our proposed model can serve as a useful tool for the design and development of antiferroelectric and antiferroelectric-like actuators.

KEYWORDS

Phenomenological, Antiferroelectric, Antiferroelectric-like, Actuator

1 | INTRODUCTION

Piezoelectric actuator has been being an essential application in microelectromechanical coupling systems (MEMS) due to excellent coupling coefficients of piezoelectric materials such as lead zirconate titanate (PZT). Moreover, PZT also displays ferroelectric (FE) behavior, which refers to the presence of spontaneous polarization in the absence of external electric field and its ability to be switched under external stimuli such as electric field or mechanical stress. An analogous behavior is observed in the anti-ferroelectric (AFE) effect, where the electromechanical coupling becomes evident as the material transitions from an anti-ferroelectric to a ferroelectric phase. However, in anti-ferroelectric materials, often characterized with double polarization-versus-electric field (P-E) hysteresis loop, the macroscopic net spontaneous polarization at zero external fields is zero or negligible due to the opposite orientation of adjacent dipole moments^{1,2}. In terms of actuator application, AFE actuators are particularly intriguing compared to ferroelectric-based device because large induced electro-strain can be generated from the external electric field, in which the extra strain is provided from the extrinsic volume change effect³. Moreover, the electro-strain in AFE actuators is often experiencing abrupt generation of deformation, making them compelling for digital on-off actuation switch^{4,5}. It is also noteworthy to mention that AFE materials are generally more attractive in memory and energy storage applications as it offers higher charge density and larger recoverable energy from the double P-E hysteresis loop, as such many lead zirconate (PbZrO₃ or PZ)-based materials have been the main candidates for these applications for the past decades². Despite of owning interesting property, PZ-based AFE materials have not been widely adopted in MEMS industry because of the incompatibility with complementary metal oxide semiconductor (CMOS) technology and lead-containing

feature³. Antiferroelectric behavior does not only manifest in PZ-based materials, on the other parallel body of work, Hafnium oxide (HfO₂) and Zirconium oxide (ZrO₂) have already been used in semiconductor technology as high dielectric materials for decades until the recent discovery of ferroelectric behavior in Silicon-doped Hafnium oxide (Si:HfO₂)⁶ and solid solution of Hafnium Zirconium oxide (Hf_xZr_{1-x}O₂ or HZO)⁷ has re-ignited research interest in these material structures. Unlike the perovskite material structure, e.g. PZT, ferroelectric behavior in fluorite structure of HZO can be achieved by stabilizing the orthorhombic phase with dopants such as Si, Al, Zr, La, Y (see³ and references therein). Interestingly, high dopant density can even result in a pinched P-E hysteresis loop, resembling the double loops of AFE materials^{8,9}. However, the AFE-like origin of such pinched loop is argued to be the result of phase transition between the non-polar tetragonal phase and the polar orthorhombic phase in contrast to the anti-parallel spontaneous polarization of two adjacent unit-cells in AFE materials. Here, the term AFE-like is used to indicate the different origins of the double hysteresis loop as compared to PZ-based material. It should be noted that the AFE-like behavior can also be rooted from other causes, such as space charges at the grain boundary or defect dipole¹⁰. Nevertheless, both AFE and AFE-like behavior is of great importance, not only as an essential new candidate for field-effect transistor^{1,11,3}, but also for actuator, transducer and energy harvester^{12,13}. Therefore, it is necessary to develop robust computational model for these innovative materials, which is the motivation of this paper.

Until now, there have been various computational models for ferroelectric actuator made of PZT. In the context of continuum mechanics, these models can be divided into two main categories. The first class of ferroelectricity modeling is based on micro-electromechanics, in which the polarization switching in each grain is described via the discrete transformation from one domain invariant into the other based on the energy-switching criteria for single crystalline¹⁴ and polycrystalline ferroelectric materials¹⁵. Although the underlying physics of domain switching was successfully modeled by finite element method^{16,17}, large number of grains is required for accuracy, leading to very high computational cost and rendering the micro-electromechanics approach impractical for structural analysis. On the other hand, in the second approach based on phenomenological observation, the ferroelectric switching is characterized through a set of internal variables such as irreversible polarization and strain, demonstrating more favorable computational effort. In this approach, the macroscopic response where the predicting hysteresis effect of electric displacement or mechanical strain is described through fitted functions that usually derived from the choice of free energy density within a thermodynamic consistency framework^{18,19,20} such that the evolution of internal variables satisfy the second-law of thermodynamics through the introduction of dissipation potential^{21,22,23}. In our previous work, we have also proposed a simplified thermodynamic-consistency model for the prediction of ferroelectric micro-actuator^{24,25}. It should be noted that under the assumption of actuator working range, thermodynamic laws is not necessarily enforced as in the case of Preisach operator-based modeling approach^{26,27}, in which the irreversible polarization is represented by a Preisach-operator²⁸ as a nonlinear function of history of applied electric field and subsequently defined the electromechanical coupling coefficient. Due to its practicability, Preisach-based model is more suitable for structural elements actuator such as beams and shells^{29,30}.

Despite of its promising potential, the computational modeling of AFE or AFE-like actuators is scarce in comparison to their FE counterpart. A noteworthy exception work based on micro-electromechanics model was proposed in³¹, in which the AFE to FE phase transition is described by the phase change between quasi-cubic to tetragonal. In addition, phase-field method has also been employed to model the microstructure evolution of ferroelectric and antiferroelectric materials, since the double loop hysteresis can be resolved by extending higher-order terms in the Landau-Ginsburg-Devonshire energy³². Nevertheless, the phase-field method also suffers the same computational cost inefficiency similar to the micro-electromechanics approach. Hence, from the modeling point of view, it is necessary to develop a phenomenological model for AFE or AFE-like actuator, which is the objective of this paper. In this work, the exclusive double hysteresis phenomenon is characterized by hyperbolic tangent functions to describe the switching polarization, which has been successfully employed in ferroelectric field transistor^{33,34} in recent years. By fitting the coefficients in the switching polarization function, completely and partially pinched hysteresis loop can be achieved, offering the flexibility to capture both AFE and AFE-like phenomenon. Subsequently, sharing the same spirit of Preisach-based method^{26,27}, the double switching polarization will be treated as a dependent variable of the piezoelectric coupling tensor as well as the irreversible strain tensor in the constitutive laws, from which the electric field-induced deformation of AFE and AFE-like actuator can be determined from finite element method. This paper is structured as following: in Section 2, we will briefly present the general description of electromechanical coupling governing equations with the decomposition of total strain and polarization into reversible and irreversible components. The description of irreversible polarization will be given in Section 2, which also introduces the nonlinearity to the boundary value problem. Section 3 will present the finite element implementation including the linearization and discretization forms, from which nonlinear solutions can be obtained. Numerical results of the proposed method will be demonstrated in Section 4, presenting the responses of AFE and AFE-like actuators. Finally, some concluding remarks will be drawn in Section 5.

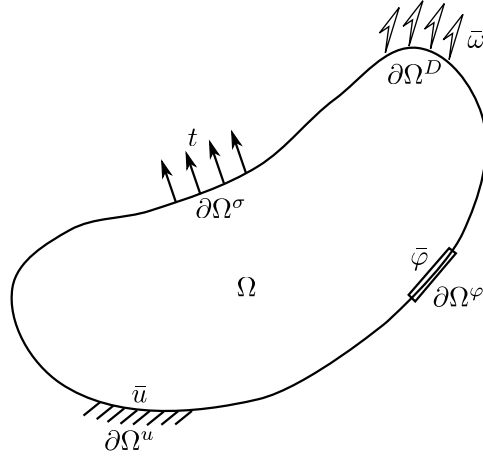


FIGURE 1 Schematic of a continuum AFE or AFE-like body.

2 | THEORETICAL FORMULATION

This section will present the theoretical formulation of our proposed AFE and AFE-like actuator model. The continuum description of piezoelectric material is presented, emphasizing on the decomposition of total mechanical strain and polarization into reversible and irreversible components, in which irreversible polarization determines the hysteresis behavior. Subsequently, a phenomenological model of irreversible polarization describing AFE and AFE-like response is presented. The established constitutive relations are then cast into finite element framework from which numerical solutions of AFE and AFE-like actuator can be obtained.

2.1 | Continuum description

Let us consider a AFE or AFE-like solid Ω , bounded by the boundary $\partial\Omega$ such that $\partial\Omega = \partial\Omega^u \cup \partial\Omega^\varphi = \partial\Omega^\sigma \cup \partial\Omega^q$ and $\partial\Omega^u \cap \partial\Omega^\sigma = \emptyset$, $\partial\Omega^\varphi \cap \partial\Omega^q = \emptyset$ as shown schematically in Fig. 1. The sub-boundary domain $\partial\Omega^u$ and $\partial\Omega^\varphi$ are the portion of boundary on which displacement and electric potential are prescribed, respectively, whereas $\partial\Omega^\sigma$ and $\partial\Omega^q$ are the boundary subjected to mechanical traction force $\mathbf{t} = \boldsymbol{\sigma} \cdot \mathbf{n}$ and electrical charge $\mathbf{q} = -\mathbf{D} \cdot \mathbf{n}$, respectively, with \mathbf{n} denotes the unit normal vector, $\boldsymbol{\sigma}$ and \mathbf{D} are the stress tensor and electric displacement vector. In the absence of body force and body charge, the stress and electric displacement are governed by the following equations²⁷

$$\nabla \cdot \boldsymbol{\sigma} = \mathbf{0}, \text{ in } \Omega, \quad (1a)$$

$$\nabla \cdot \mathbf{D} = \mathbf{0}, \text{ in } \Omega, \quad (1b)$$

subjected to the boundary conditions

$$\mathbf{u} = \bar{\mathbf{u}}, \quad \text{on } \partial\Omega^u, \quad (2a)$$

$$\varphi = \bar{\varphi}, \quad \text{on } \partial\Omega^\varphi, \quad (2b)$$

$$\mathbf{t} = \boldsymbol{\sigma} \cdot \mathbf{n} = \bar{\mathbf{t}}, \quad \text{on } \partial\Omega^\sigma, \quad (2c)$$

$$\mathbf{q} = \mathbf{D} \cdot \mathbf{n} = -\bar{\mathbf{q}}, \quad \text{on } \partial\Omega^q, \quad (2d)$$

in which $\nabla = \frac{\partial}{\partial x_i}$ is the differential operator and the $(\bar{\cdot})$ denotes the prescribed variables. Besides, the kinematic variables (total) strain ε and electric field \mathbf{E} can be obtained from displacement and electric potential fields, respectively, as following

$$\varepsilon = \frac{1}{2}(\nabla \mathbf{u} + \mathbf{u} \nabla), \quad (3a)$$

$$\mathbf{E} = -\nabla \varphi, \quad (3b)$$

for small deformation assumption of ceramic piezoelectric materials²⁷. Following²⁶ and reference therein, to describe the hysteresis effect, it is possible to decompose the total strain and polarization into reversible and irreversible parts as follows

$$\varepsilon = \varepsilon^r + \varepsilon^i, \quad (4a)$$

$$\mathbf{P} = \mathbf{P}^r + \mathbf{P}^i, \quad (4b)$$

where ε^r and \mathbf{P}^r are reversible strain and polarization, respectively, whereas ε^i and \mathbf{P}^i denote irreversible strain and polarization, respectively. The reversible components attribute the the linear response in the constitutive relationships, meanwhile the irreversible components represent nonlinear hysteresis behavior of the material response. As a result, the constitutive laws of the Cauchy stress $\boldsymbol{\sigma}$ and electric displacement \mathbf{D} in nonlinear piezoelectricity read²⁷

$$\boldsymbol{\sigma} = \mathbf{C} : (\varepsilon - \varepsilon^i(\mathbf{P}^i)) - \mathbf{e}(\mathbf{P}^i) \cdot \mathbf{E}, \quad (5a)$$

$$\mathbf{D} = \mathbf{e}(\mathbf{P}^i) : (\varepsilon - \varepsilon^i(\mathbf{P}^i)) + \kappa \cdot \mathbf{E} + \mathbf{P}^i, \quad (5b)$$

showing the central role of the irreversible polarization \mathbf{P}^i in material response. Particularly, by adopting the assumption of volume preservation during domain switching event in ferroelectric material^{27,29}, the irreversible strain ε^i is related to the irreversible polarization as follows

$$\varepsilon^i = \frac{3}{2} \varepsilon^s \frac{\|\mathbf{P}^i\|}{P^s} (\mathbf{e}^P \otimes \mathbf{e}^P - \mathbf{I}), \quad (6)$$

where ε^s and P^s denote the saturated strain and polarization coefficients, respectively, \mathbf{e}^P is the polarization direction (in this work the polarization is assumed to be the same as the direction of applied electric field, i.e. $\mathbf{e}^P = [0, 0, 1]$) and \mathbf{I} is the second-order identity tensor. Note that with the assumption of \mathbf{e}^P , the model is limited to uni-axial loaded actuator²⁷. Furthermore, based on the observation that piezoelectric effect only appears when the material is poled and disappears under the vanishing of switching polarization, the piezoelectric tensor is also assumed to be a function of irreversible polarization as follows

$$\mathbf{e}(\mathbf{P}^i) = \frac{\|\mathbf{P}^i\|}{P^s} \mathbf{e}, \quad (7)$$

where \mathbf{e} is the (linear) piezoelectric tensor. The magnitude of irreversible polarization often results in the P_z^i component, rendering the model of a fixed polarization direction under uni-axial electric loading²⁷. This restriction greatly simplifies the derivation of tangent stiffness moduli as will be shown in the next sections, but for now let us present the model of irreversible polarization for the double hysteresis characteristic of AFE and AFE-like materials.

2.2 | Mathematical description of irreversible polarization

Phenomenological modeling approach assumes that material response can be represented by a mathematical model, which is then calibrated to fit with observation. In such manner, ferroelectric polarization switching was modeled by hysteresis operators such as the Preisach-operator³⁵. However, the Preisach-operator is not applicable for AFE and AFE-like material response that is characterized by double hysteresis loop. In this work, we adopt the irreversible polarization model from^{33,34} as follows

$$P^i(E) = \frac{P^s}{2} \left[\tanh \left[\frac{E - E_c^2}{2\gamma} \right] - \tanh \left[\frac{-E - E_c^1}{2\gamma} \right] \right], \quad (8)$$

with

$$\gamma = \frac{E_c}{\log \left(\frac{1+P^r/P^s}{1-P^r/P^s} \right)}, \quad (9)$$

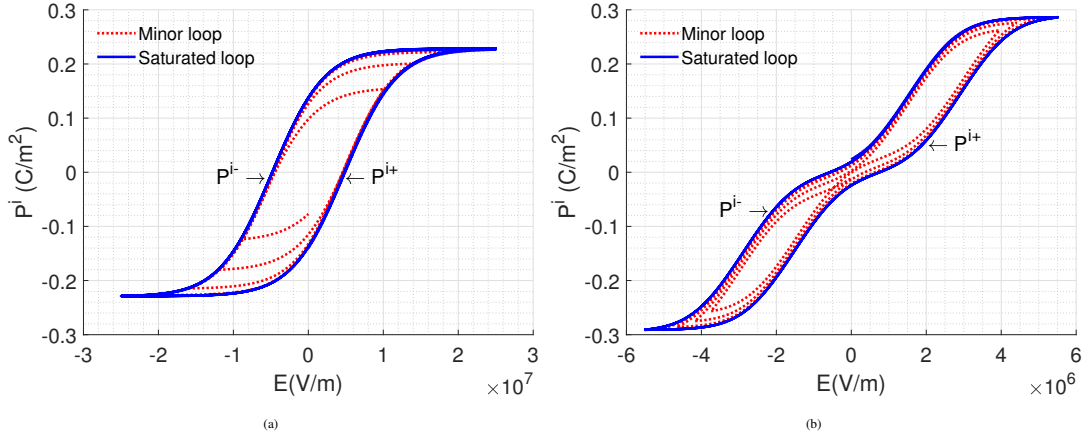


FIGURE 2 Examples of irreversible polarization. The saturated polarization loop for increasing and decreasing electric field, P^{i+} and P^{i-} , respectively. (a) Ferroelectric behavior. (b) Antiferroelectric-like behavior.

where E is the applied electric field, P^r and P^s are remanent and saturated polarization, respectively; E_c , E_c^1 and E_c^2 are the coercive electric fields. Furthermore, the field-dependent polarization loop is separated into two branches, i.e. increasing and decreasing electric field

$$P^{i+}(E) = P^i(E), \quad \text{for increasing } E, \quad (10)$$

$$P^{i-}(E) = -P^i(-E), \quad \text{for decreasing } E. \quad (11)$$

The above model is extended from Miller's nonlinear capacitor model³⁶, in which only one hyperbolic tangent function is required to produce ferroelectric polarization switching, i.e. single hysteresis loop as shown in Fig. 2a, meanwhile the additional hyperbolic tangent function in this work offers a possibility to capture the AFE and AFE-like behavior as shown in Fig. 2b. It is important to note that such polarization corresponds to the fully saturated state, i.e. when the electric field is large enough to align all dipole moments. In realistic situation, the applied electric field is not necessarily uniform or alternating between positive and negative signals. The arbitrary electric signal can lead to unsaturated switching polarization, which displays as the minor loop within the major hysteresis loop as shown in Fig. 2. To accommodate such scenarios for AFE and AFE-like actuator, we adapt the strategy proposed in³⁷, where the minor loop is represented by the rate of change of irreversible polarization as

$$\frac{\partial P^{i,minor}}{\partial E} = \Gamma \frac{\partial P^i(E)}{\partial E}, \quad (12)$$

where P^i is the saturated polarization at applied electric field E as defined in Eq. (8), Γ is a decay function given as

$$\Gamma = 1 - \tanh \left[\sqrt{\frac{P^{i,minor} - P^i}{\xi P^s - P^{i,minor}}} \right], \quad (13)$$

with $\xi = \pm 1$ for increasing and decreasing electric field, respectively. By virtue of Eq. (13), the rate of change of the minor loop approaches the change of the major loop when $P^{i,minor} \rightarrow P^i$, hence $\Gamma \rightarrow 1$. On the other hand, the rate of change of the minor loop polarization becomes insignificant when $\|P^{i,minor}\| \rightarrow \|\xi P^s\|$. In the original work³⁷, the minor hysteresis loop was obtained for ferroelectric irreversible polarization as demonstrated in Fig. 2a, whereas in this current paper, we speculate the minor hysteresis loop of AFE and AFE-like materials can be governed by the same decay function and result in the minor loops illustrated by the dotted lines in Fig. 2b. As emphasized in³⁷, the decay function Γ is simply a mathematical convenience to represent the smaller rate of change of the minor polarization as compared to saturated one, hence it bears no physical meaning as such alternative form of decay function Γ can be used to better fit with the observation.

More importantly, by tuning the AFE parameters E_c , E_c^1 and E_c^2 , various shapes of AFE and AFE-like hysteresis can be obtained. Fig. 3 demonstrates different types of P-E loop can be obtained from Eq. (8) for different values of E_c , E_c^1 and E_c^2 . These loops include the 'square' and 'slanted' double loop (Fig. 3a and 3b) that are often found in AFE PZ-based materials, as well as a pinched hysteresis loop in AFE-like HZO-based material. Interestingly, when one of the coercive field E_c^1 vanishes and the other

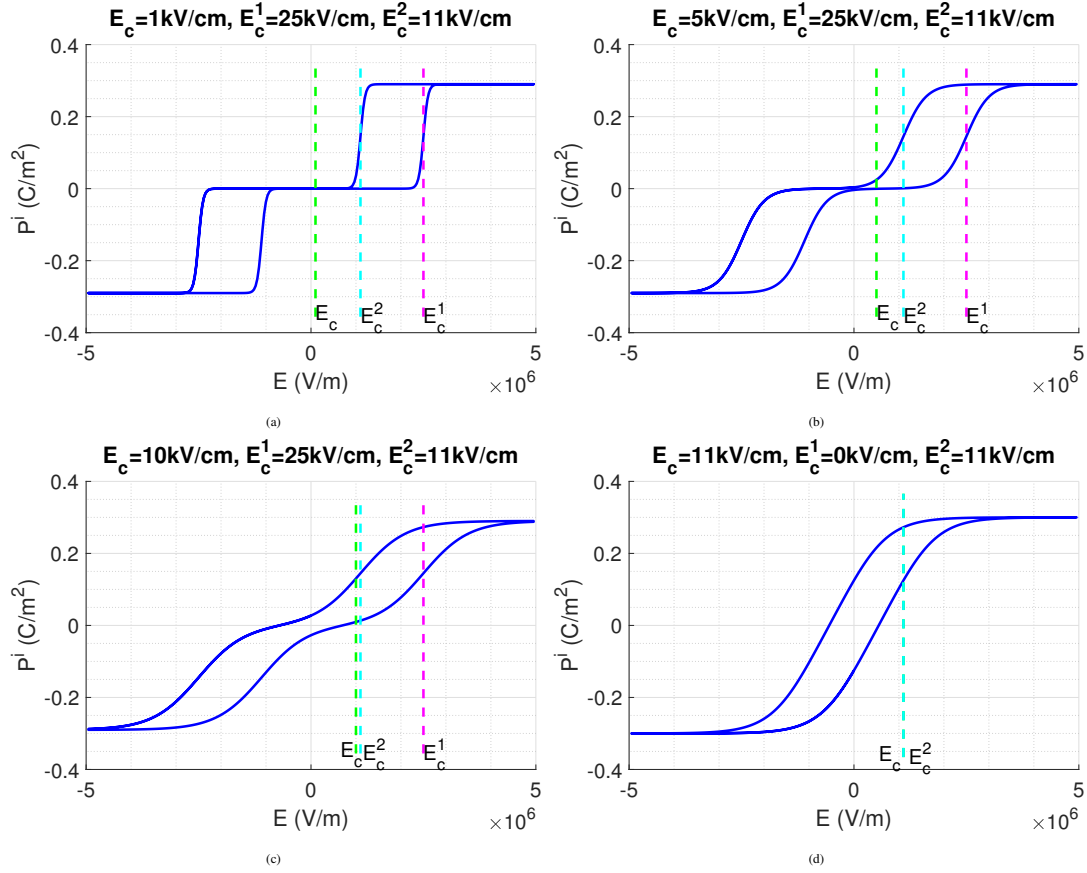


FIGURE 3 Irreversible polarization model for various combinations of coercive field parameters results in (a) square double loop; (b) slanted double loop; (c) pinched single loop and (d) single loop.

two coercive fields coincide, a single hysteresis loop of ferroelectric behavior can be also retrieved. As can be seen from Fig. 3, lower value of E_c produces a P-E loop with a more dominant AFE phase at low electric field, whereas increasing E_c can induce the phase transition from AFE to FE at lower electric field and further increased E_c generates a resemble of pinched hysteresis loop at zero electric field. It should be remarked that the production of AFE and AFE-like hysteresis loop is purely from the hyperbolic tangent functions rather than physical causes as emphasized in³⁶. Furthermore, the generated switching polarization is aligned with the applied electric field, complementing with the uni-axial electrical loading assumption in the previous section.

To this end, with the nonlinear expression of irreversible polarization for arbitrary applied electric field by Eq. (8) and Eq. (12), the continuum description AFE and AFE-like actuator is complete. It is of great importance to point out that while the adopted irreversible polarization models were mainly employed to capture P-E hysteresis in previous works^{33,34,36,37} for nonlinear ferroelectric and anti-ferroelectric capacitors and transistors, in our current work the irreversible polarization model is further exploited to capture induced deformation from applied electric field. For this purpose, the irreversible polarization will be cast into the continuum description of AFE and AFE-like solid such that the boundary value problem can be numerically solved in finite element framework in the next section.

3 | FINITE ELEMENT FORMULATION

In order to derive the finite element formulation of AFE and AFE-like actuator, let us first consider the total potential of piezoelectric solid defined as follows³⁸

$$\pi(\varepsilon, \mathbf{E}) = \frac{1}{2} \int_{\Omega} \boldsymbol{\sigma} : (\boldsymbol{\varepsilon} - \boldsymbol{\varepsilon}^i) d\Omega - \frac{1}{2} \int_{\Omega} \mathbf{D} \cdot \mathbf{E} d\Omega - \int_{\partial\Omega^{\sigma}} \mathbf{u} \cdot \bar{\mathbf{t}} dA + \int_{\partial\Omega^D} \varphi \bar{\omega} dA, \quad (14)$$

in which the mechanical stress $\boldsymbol{\sigma}$ and electric displacement \mathbf{D} are defined in Eq. (5). Upon employing variational principle on Eq. (14), the weak-form can be obtained as

$$\delta\pi(\boldsymbol{\varepsilon}, \mathbf{E}) = \int_{\Omega} \delta\boldsymbol{\varepsilon} : \boldsymbol{\sigma} \, d\Omega - \int_{\Omega} \delta\mathbf{E} \cdot \mathbf{D} \, d\Omega - \int_{\partial\Omega^{\sigma}} \delta\mathbf{u} \cdot \bar{\mathbf{t}} \, dA + \int_{\partial\Omega^D} \delta\varphi \bar{\omega} \, dA = 0. \quad (15)$$

Based on Eq. (5) and Eq. (8), the integrands in Eq. (15) are nonlinear, thus can be then linearized as

$$\delta\pi(\boldsymbol{\varepsilon}, \mathbf{E}) + \Delta\delta\pi(\boldsymbol{\varepsilon}, \mathbf{E}) = 0, \quad (16)$$

in which the linearization of the variation of the internal energy is given as

$$\begin{aligned} \Delta\delta\pi(\boldsymbol{\varepsilon}, \mathbf{E}) &= \int_{\Omega} \delta\boldsymbol{\varepsilon} : \frac{\partial\boldsymbol{\sigma}}{\partial\boldsymbol{\varepsilon}} : \Delta\boldsymbol{\varepsilon} \, d\Omega + \int_{\Omega} \delta\boldsymbol{\varepsilon} : \frac{\partial\boldsymbol{\sigma}}{\partial\mathbf{E}} \cdot \Delta\mathbf{E} \, d\Omega \\ &\quad - \int_{\Omega} \delta\mathbf{E} \cdot \frac{\partial\mathbf{D}}{\partial\boldsymbol{\varepsilon}} : \Delta\boldsymbol{\varepsilon} \, d\Omega - \int_{\Omega} \delta\mathbf{E} \cdot \frac{\partial\mathbf{D}}{\partial\mathbf{E}} \cdot \Delta\mathbf{E} \, d\Omega \\ &= \int_{\Omega} \delta\boldsymbol{\varepsilon} : \mathbb{C} : \Delta\boldsymbol{\varepsilon} \, d\Omega + \int_{\Omega} \delta\boldsymbol{\varepsilon} : \mathbb{E}^{\sigma} \cdot \Delta\mathbf{E} \, d\Omega \\ &\quad - \int_{\Omega} \delta\mathbf{E} \cdot \mathbb{E}^D : \Delta\boldsymbol{\varepsilon} \, d\Omega - \int_{\Omega} \delta\mathbf{E} \cdot \mathbb{K} \cdot \Delta\mathbf{E} \, d\Omega, \end{aligned} \quad (17)$$

where the tangent elastic tensor \mathbb{C} , the tangent piezoelectric tensors \mathbb{E}^{σ} and \mathbb{E}^D are, and the tangent dielectric tensor \mathbb{K} can be determined from the constitutive laws Eq. (5). Specifically, the tangent elastic tensor \mathbb{C} and the tangent piezoelectric tensor \mathbb{E}^D can be obtained as

$$\mathbb{C} = \mathbf{C}, \quad (18a)$$

$$\mathbb{E}^D = \mathbf{e}(\mathbf{P}^i(\mathbf{E})), \quad (18b)$$

which are the elastic tensor and the irreversible polarization-dependent linear piezoelectric tensor Eq. (7), respectively. On the other hand, in combination with Eq. (8), the tangent piezoelectric tensor \mathbb{E}^{σ} and the tangent dielectric tensor \mathbb{K} can be obtained by using chain rule as following

$$\mathbb{E}^{\sigma} = \frac{\partial\boldsymbol{\sigma}}{\partial\mathbf{E}} = \mathbf{C} : \frac{\partial\boldsymbol{\varepsilon}^i}{\partial\mathbf{E}} - \frac{\partial\mathbf{e}}{\partial\mathbf{E}} \cdot \mathbf{E} - \mathbf{e} = \mathbf{C} : \frac{\partial\boldsymbol{\varepsilon}^i}{\partial\mathbf{P}^i} \cdot \frac{\partial\mathbf{P}^i}{\partial\mathbf{E}} - \frac{\partial\mathbf{e}}{\partial\mathbf{P}^i} \cdot \frac{\partial\mathbf{P}^i}{\partial\mathbf{E}} \cdot \mathbf{E} - \mathbf{e}, \quad (19a)$$

$$\mathbb{K} = \frac{\partial\mathbf{D}}{\partial\mathbf{E}} = \frac{\partial\mathbf{e}}{\partial\mathbf{E}} : (\boldsymbol{\varepsilon} - \boldsymbol{\varepsilon}^i) - \mathbf{e} \frac{\partial\boldsymbol{\varepsilon}^i}{\partial\mathbf{E}} + \boldsymbol{\kappa} + \frac{\partial\mathbf{P}^i}{\partial\mathbf{E}}, \quad (19b)$$

where

$$\frac{\partial\mathbf{e}}{\partial\mathbf{E}} = \frac{3}{2} \frac{1}{P_s} \frac{\partial\|\mathbf{P}^i\|}{\partial\mathbf{E}} (\mathbf{e}^P \otimes \mathbf{e}^P - \mathbf{I}), \quad (20)$$

is obtained from Eq. (7). It can be seen that the tangent moduli in Eq. (19) can be computed from the rate of change of irreversible polarization with respect to applied electric field using Eq. (8) and Eq. (12). As mentioned in previous section, the current work aims to simulate the uni-axial actuator, in which the applied electric field direction is aligned with the induced polarization, i.e. E_z and P_z^i , while other components of the electric field and irreversible polarization vectors are zeros, further simplifying the computation of tangent moduli in Eq. (19). Furthermore, it should be noted that, in contrast to thermodynamic consistent model in ferroelectricity²⁵ where the irreversible polarization is determined from dissipation potential, the evolution of irreversible polarization in the current work is given explicitly from Eq. (8) and Eq. (12) as a function of electric field profile. Although this approach does not enforce thermodynamic principle, it is still applicable for modeling actuator in working range as shown in²⁷ where Preisach-operator is employed and solved numerically by quasi-Newton method. Similarly, in order to solve the boundary value problem numerically, we employ finite element discretization to approximate displacement and electric potential fields, \mathbf{u} and φ , respectively, as well as their variations as follows

$$\mathbf{u} = \mathbf{N}^u \hat{\mathbf{u}}, \quad \delta\mathbf{u} = \mathbf{N}^u \delta\hat{\mathbf{u}}, \quad (21a)$$

$$\varphi = \mathbf{N}^{\varphi} \hat{\varphi}, \quad \delta\varphi = \mathbf{N}^{\varphi} \delta\hat{\varphi}, \quad (21b)$$

where \mathbf{N}^u and \mathbf{N}^ϕ are the matrices contains basis shape functions, $\hat{\mathbf{u}}$ and $\hat{\phi}$ are the nodal displacement and electric potential, respectively. Subsequently, total strain and electric field can be approximated as

$$\boldsymbol{\varepsilon} = \mathbf{B}^u \hat{\mathbf{u}}, \quad \delta \boldsymbol{\varepsilon} = \mathbf{B}^u \delta \hat{\mathbf{u}}, \quad (22a)$$

$$\mathbf{E} = \mathbf{B}^\varphi \hat{\phi}, \quad \delta \mathbf{E} = \mathbf{B}^\varphi \delta \hat{\phi}, \quad (22b)$$

where \mathbf{B}^u and \mathbf{B}^φ are the matrices of derivative of shape functions.

Upon substituting Eq. (22) into Eq. (15), the discretization of the variation of the internal energy can be obtained as

$$\delta \pi^h = \int_{\Omega} \left[\delta \hat{\mathbf{u}}^T (\mathbf{B}^u)^T \boldsymbol{\sigma} - \delta \hat{\phi}^T (\mathbf{B}^\varphi)^T \mathbf{D} \right] d\Omega - \left[\int_{\partial\Omega^\sigma} (\mathbf{N}^u)^T \bar{\mathbf{t}} dA + \int_{\partial\Omega^D} (\mathbf{N}^\varphi)^T \bar{\omega} dA \right] = 0. \quad (23)$$

Similarly, the discretization form of the linearization of variation of internal energy can be obtained by substituting Eq. (22) into Eq. (17) as

$$\begin{aligned} \Delta \delta \pi^h = & \int_{\Omega} \delta \hat{\mathbf{u}}^T (\mathbf{B}^u)^T \mathbb{C} \mathbf{B}^u \Delta \hat{\mathbf{u}} d\Omega + \int_{\Omega} \delta \hat{\mathbf{u}}^T (\mathbf{B}^u)^T \mathbb{E}^\sigma \mathbf{B}^\varphi \Delta \hat{\phi} d\Omega \\ & - \int_{\Omega} \delta \hat{\phi}^T (\mathbf{B}^\varphi)^T \mathbb{E}^D \mathbf{B}^u \Delta \hat{\mathbf{u}} d\Omega - \int_{\Omega} \delta \hat{\phi}^T (\mathbf{B}^\varphi)^T \mathbb{K} \mathbf{B}^\varphi \Delta \hat{\phi} d\Omega. \end{aligned} \quad (24)$$

Finally, substituting Eq. (23) and Eq. (24) into Eq. (16) and employing the arbitrariness of test functions, the system of linear equations of incremental displacement and electric potential in each Newton-Raphson step can be obtained as follows

$$\begin{bmatrix} \mathbf{K}_t^{uu} & \mathbf{K}_t^{u\phi} \\ \mathbf{K}_t^{\phi u} & \mathbf{K}_t^{\phi\phi} \end{bmatrix} \begin{bmatrix} \Delta \hat{\mathbf{u}} \\ \Delta \hat{\phi} \end{bmatrix} = \begin{bmatrix} \mathbf{f}_u \end{bmatrix} - \begin{bmatrix} \mathbf{r}_i^u \\ \mathbf{r}_i^\varphi \end{bmatrix}, \quad (25)$$

where the stiffness matrices and force vectors can be found in details in the Appendix. Note that as the current work focuses on the actuating application, electric potential is imposed as the Dirichlet boundary conditions and the displacement field is updated during Newton-Raphson procedure as

$$\mathbf{u}_{n+1}^{k+1} = \mathbf{u}_{n+1}^k + \Delta \mathbf{u}_{n+1}, \quad (26)$$

where n and k is the time step and Newton-Raphson step, respectively, $\Delta \mathbf{u}_{n+1}$ is the incremental displacement solution of the system of linear equations Eq. (25). Note that at each time step, the irreversible polarization can be explicitly computed from its rate of change with respect to applied electric field as

$$P_{n+1}^i = P_n^i + \left. \frac{\partial P^i}{\partial E} \right|_n (E_{n+1} - E_n), \quad (27)$$

in which $\frac{\partial P^i}{\partial E}$ is determined from Eq. (8) and Eq. (12), E_{n+1} and E_n are the electric field at time step $n+1$ and n , respectively.

4 | NUMERICAL RESULTS

This section presents the numerical results from our proposed model for AFE and AFE-like materials. Specifically, we will study the induced uniaxial strain in AFE materials such as niobium-doped and lanthanum-doped lead zirconate titanate stannate (PNZST and PLZST, respectively) and compare the numerical prediction with experimental uniaxial actuation data. On the other hand, the behavior of AFE-like material will be studied in a silicon-doped hafnium oxide nano-cantilever, in which pinched-hysteresis P-E loop is compared with experimental result and from which numerical displacement can be estimated.

4.1 | Antiferroelectric actuator

In this section, we will demonstrate the capability of the proposed method in modeling anti-ferroelectric actuator. Specifically, the method will be employed to model the polarization and strain hysteresis loops and compare with experimental data of uniaxial actuation for PNZST and PLZST thick films from⁴. While both having antiferroelectric response, the two doping

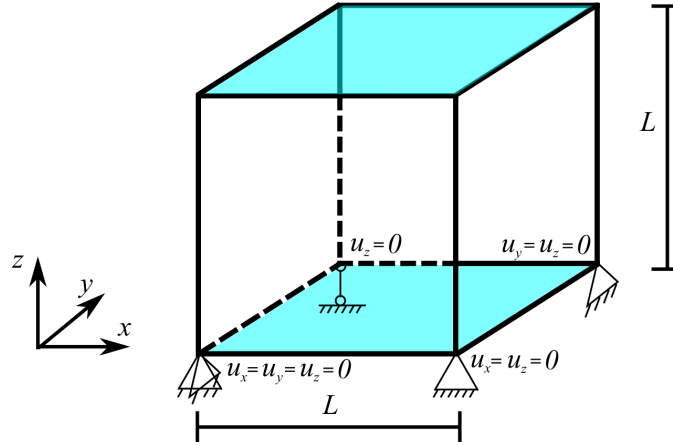


FIGURE 4 Schematic of PNZST and PLZST cube actuator of dimension $L = 1\text{ mm}$ with bottom and top electrodes. Displacement constraint is applied to allow longitudinal deformation along z -direction under applied voltage.

compositions result in different shape of polarization hysteresis loop, 'square' transition was found in PNZST whereas 'slanted' shape occurred with PLZST, which are generally challenging for computational modeling. Therefore, the objective of this example is to utilize the measured polarization loop for fitting hysteresis parameters in Eq. (8), and consequently predict the induced longitudinal strain. The desired longitudinal strain can be achieved by considering a simple geometry of a cube of dimension 1 mm consists of grounded bottom electrode on the bottom surface, whereas applying alternating voltage on the top electrode on the top surface assuming polarization direction is in z -direction. In addition, the displacement constraint of the cube sample is shown schematically in Fig. 4.

The anti-ferroelectric cube sample is assumed to have the same elastic properties as PZT-5H (similar to the assumption from⁵) for both PNZST and PLZST, while the dielectric permittivities follow the measurement from⁴ and presented in Table 1. Additionally, in order to match numerical predictions from our model with experimental results, the longitudinal piezoelectric coefficient e_{33} and the hysteresis parameters $E_c, E_c^1, E_c^2, P_r, P_s, \varepsilon^s$ are fitted and presented in Table 1.

As a result of the applied sinusoidal electric field in z -direction (as shown in Fig. 6), the induced polarization and strain hysteresis loops are shown in Fig. 5, where good agreement can be observed between numerical and measurement results. The proposed model is able to capture both 'square' and 'slanted' shape of polarization loops for both material samples. Furthermore, the induced-strain in anti-ferroelectric materials is essentially obtained, especially the electric field corresponding to the AFE to FE phase transition. However, the mechanical response when material undergoing FE to AFE phase transition was not well captured as the numerical result underpredict the induced deformation. Nevertheless, produced strain for both PNZST and PLZST are satisfactorily predicted, showing the capability of the proposed model in handling varied anti-ferroelectric behaviors.

For a closer look, we present the induced strain as a function of time step in Fig. 6. As can be seen from the insets, the PNZST sample exhibits a more abrupt deformation than that in PLZST one from time step 12 to 17 before reaching maximum deformation at saturated polarization at time step 25. Such difference at sudden deformation is related to their 'square' and 'slanted' polarization hysteresis, respectively.

4.2 | Antiferroelectric-like actuator

In this next example, we will analyze the antiferroelectric-like response of an actuator. To demonstrate numerical prediction, we consider a simple cantilever beam of silicon-doped hafnium oxide of thickness 100 nm sandwiched between two electrodes of negligible thickness and the deposited on top of a silicon layer of thickness 500 nm as shown schematically in Fig. 7. The elastic properties of the stack is given in Table 2 where isotropic elasticity is assumed for both hafnium oxide layer³⁹ and silicon substrate⁴⁰. In addition, the piezoelectric and dielectric coefficients of hafnium oxide are chosen from first-principle calculation⁴¹. Antiferroelectric-like behavior is often found in si-doped hafnium oxide^{9,42} where the polarization hysteresis exhibits a pinch at low electric field, similar to the hysteresis shape shown in Fig. 3c. To mimic such behavior, the hysteresis material parameters in Eq.(8) are chosen as, which results in a typical polarization hysteresis.

TABLE 1 Material properties of PNZST and PLZST for the problem depicted in Fig. 4. The elastic and dielectric material parameters are adapted from^{5,4}, whereas the piezoelectric and hysteresis parameters are fitted from our numerical model. Note that the coefficients are given in terms of Voigt notation for transversely isotropic material.

PNZST					PLZST				
Elastic moduli $10^9(\text{N/m}^2)$					Elastic moduli $10^9(\text{N/m}^2)$				
C_{11}	C_{12}	C_{13}	C_{33}	C_{44}	C_{11}	C_{12}	C_{13}	C_{33}	C_{44}
126	84.1	84.1	126	23	126	84.1	84.1	126	23
Piezoelectric					Piezoelectric				
$e_{33}(\text{C/m}^2)$					$e_{33}(\text{C/m}^2)$				
9					2				
Relative dielectric permittivity					Relative dielectric permittivity				
κ_{33}					κ_{33}				
283					434				
AFE parameters					AFE parameters				
$P_r(\text{C/m}^2)$	$P_s(\text{C/m}^2)$	ε^s			$P_r(\text{C/m}^2)$	$P_s(\text{C/m}^2)$	ε^s		
0.22	0.23	0			0.1	0.11	0		
$E_c(\text{MV/m})$	$E_c^1(\text{MV/m})$	$E_c^2(\text{MV/m})$			$E_c(\text{MV/m})$	$E_c^1(\text{MV/m})$	$E_c^2(\text{MV/m})$		
1.8	9.3	15			3	16.5	19		

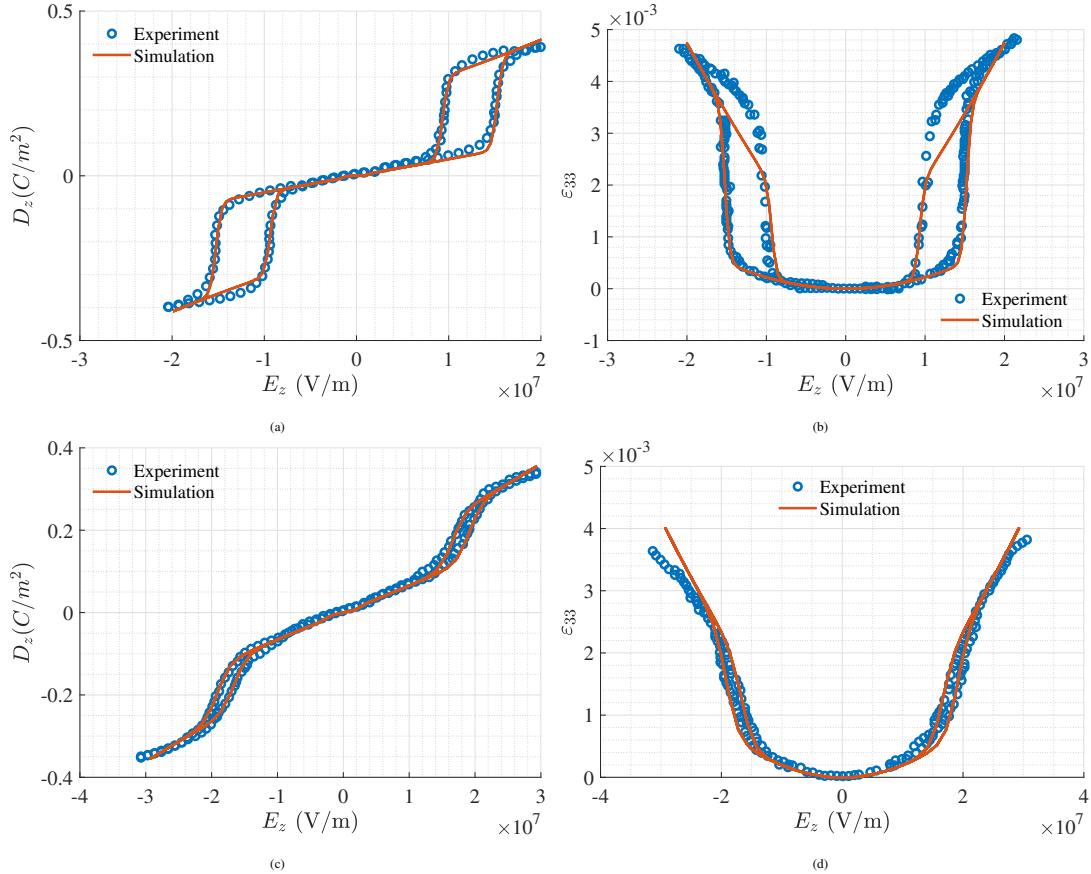


FIGURE 5 Comparison between simulation and experiment from⁴. (a-b) Polarization and strain hysteresis of PNZST. (c-d) Polarization and strain hysteresis of PLZST.

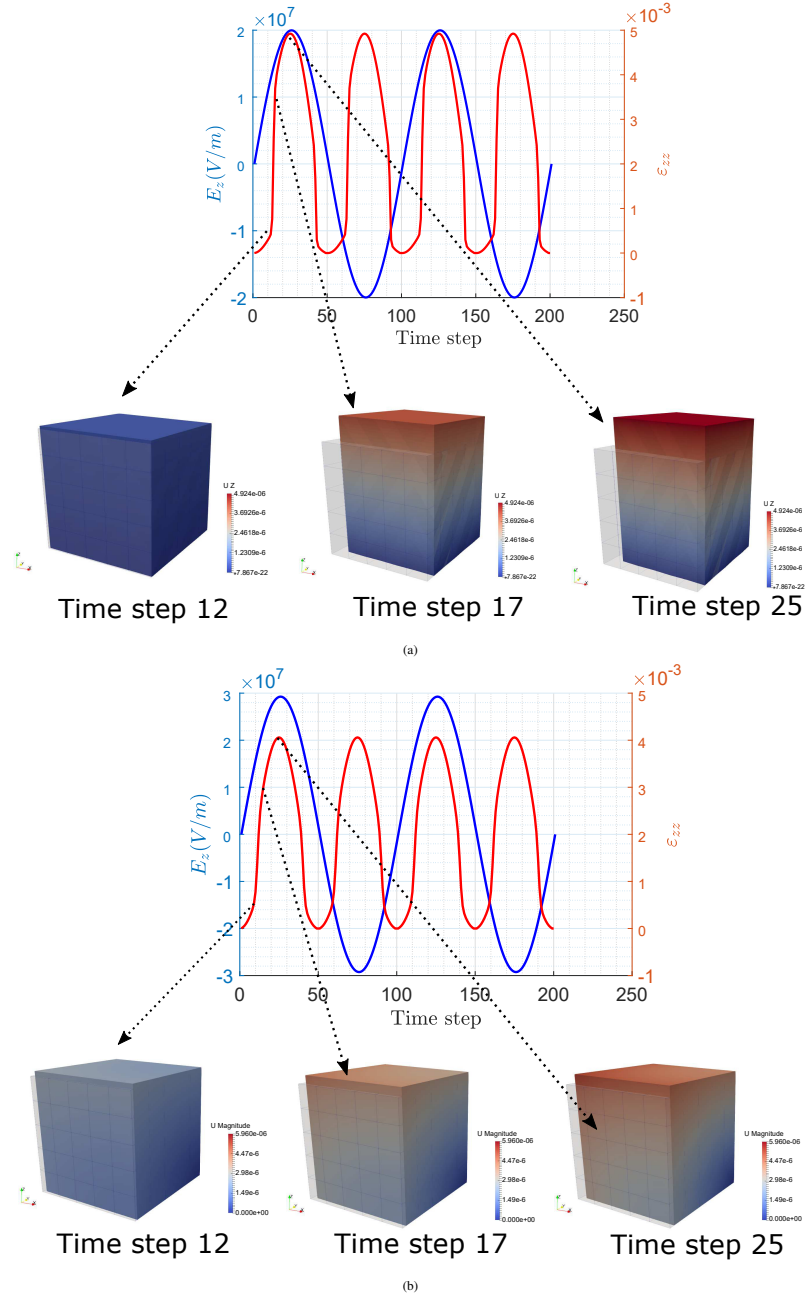


FIGURE 6 Uniaxial deformation of (a) PNZST and (b) PLZST sample for sinusoidal applied electric field E_z (blue curve). Top figure shows the displacement of the top surface of the sample, meanwhile the magnitude displacement u_z distribution snapshots at time step 12, 17 and 25 (corresponding to the electric field at E_c , E_c^1 and E_{max}) shown the bottom figures.

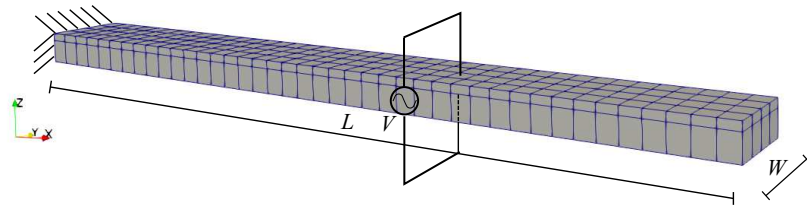


FIGURE 7 Schematic of AFE-like nano-cantilever of length $L = 10 \mu\text{m}$ and width $W = 1 \mu\text{m}$, subjected to voltage across applied on the electrodes.

TABLE 2 Material properties of the multilayer micro-actuator depicted in Fig. 7. HfO_2 and Si are assumed be isotropic elastic materials^{39,40}. The piezoelectric and dielectric permittivity of HfO_2 are adopted from first principle calculation⁴¹ whereas AFE parameters are fitted from numerical results.

HfO ₂ layer						
Young's modulus (10 ⁹ N/m ²)		Poisson ratio		Piezoelectric constants (C/m ²)		
<i>Y</i>		<i>ν</i>		<i>e</i> ₃₁	<i>e</i> ₃₃	<i>e</i> ₁₅
240		0.3		-1.1	-1.44	-0.2
Relative dielectric permittivity		AFE parameters				
<i>κ</i> ₁₁	<i>κ</i> ₃₃	<i>P_r</i> (C/m ²)	<i>P_s</i> (C/m ²)	<i>E_c</i> (MV/m)	<i>E_c</i> ¹ (MV/m)	<i>E_c</i> ² (MV/m)
40	40	0.2	0.22	100	70	190
Silicon layer						
Young's modulus (10 ⁹ N/m ²)		Poisson ratio				
<i>Y</i>		<i>ν</i>				
169		0.064				

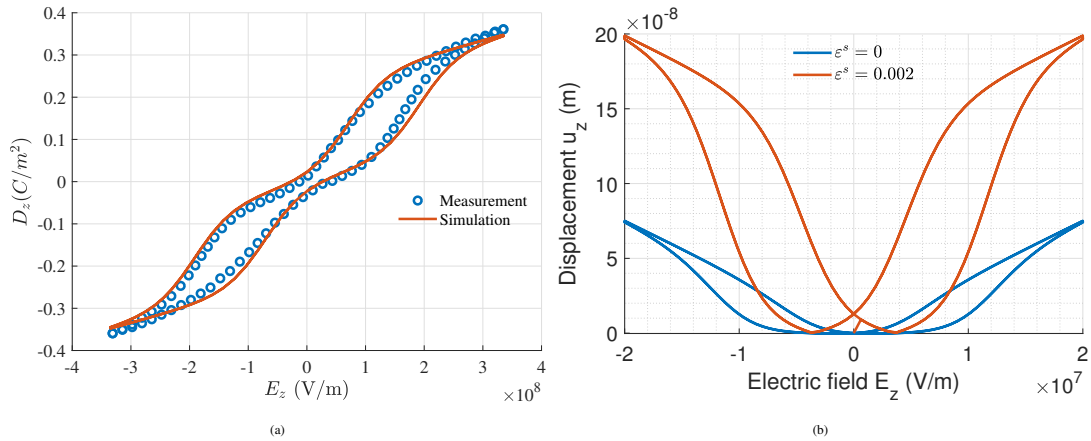


FIGURE 8 Polarization and displacement hysteresis loops in HfO nano-cantilever described in Fig. 7. (a) P-E hysteresis loop, measurement polarization from⁴². (b) Numerical displacement hysteresis loop at the tip of the beam for different saturated strain coefficient ϵ^s .

The AFE-like cantilever is modeled by linear hexahedral element as shown in Fig. 7, where the displacements are constrained at $x = 0$, the bottom and top surfaces of the hafnium layer are subjected to voltage difference, to mimic the bottom and top electrode electrical conditions. In order to compare the numerical results with measured data, an sinusoidal voltage of 33.53 V is applied on the top electrode under the quasi-static assumption. As a result, the polarization and strain hysteresis loops can be obtained and presented in Fig. 8. Fig. 8a shows a good agreement between predicted and measured electric displacement. Additionally, the mechanical response of AFE-like actuator is also obtained, however due to lacking of experimental data, we choose to study the influence of saturated strain coefficient ϵ^s , which was fitted to zero in the case of AFE actuator in previous example. For the AFE-like actuator, numerical displacement at the tip of the beam when $\epsilon^s = 0$ and $\epsilon^s = 0.002$ is presented in Fig. 8b, showing a great influence of ϵ^s on the induced deformation of AFE-like actuator where maximum displacement is 75 nm and 200 nm, respectively.

Furthermore, the mechanical displacement of the AFE-like actuator under non-uniform applied electric field is investigated. Specifically, the top electrode of the cantilever beam is subjected to bipolar and unipolar applied electric field with the maximum voltage magnitude of 33.53 V as shown in Fig. 9a and Fig. 9b, respectively. While the first triangular waveforms, corresponding to

maximum applied voltage, result in the saturated major hysteresis loop similar to previous uniform applied field. The decreasing electric field magnitude induces minor hysteresis loops that are confined in the major loops as shown in Figs. 9c and 9d for electric displacement D_z . Consequently, the minor loops of polarization hysteresis lead to the minor loops of the beam tip displacement shown in Figs. 9e and 9f, demonstrating the capability of our proposed model for capturing mechanical response of AFE-like actuator for arbitrary input signal.

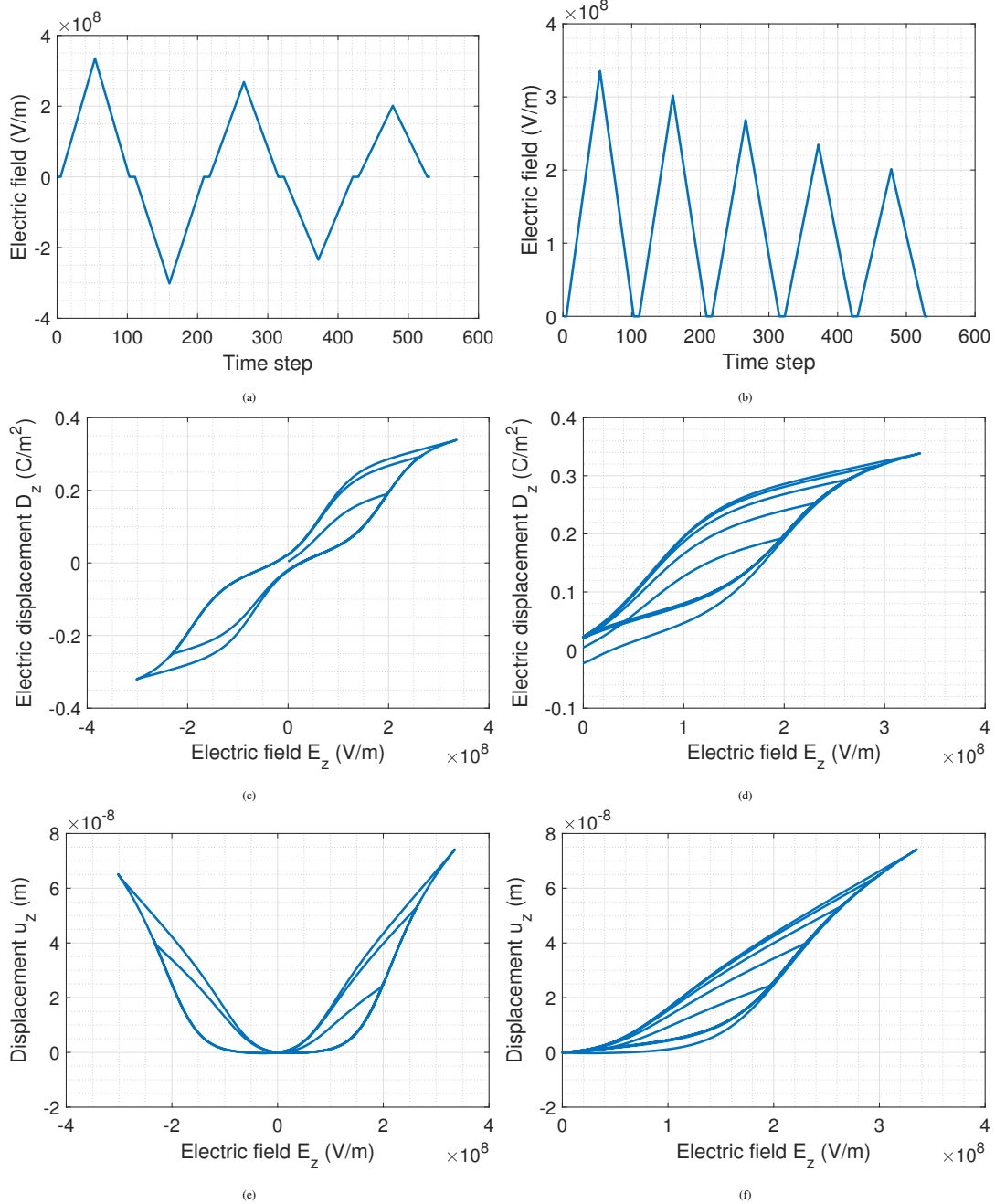


FIGURE 9 Minor hysteresis loops modeling. (a,b) Decreasing bipolar and unipolar electric field. (c,d) Minor electric displacement loops under bipolar and unipolar electric field. (e,f) Minor displacement loops (at the beam tip) under bipolar and unipolar electric field.

5 | CONCLUSIONS

In this paper, we have proposed a computational model of antiferroelectric-like actuator. The core ingredient of the proposed model is the expression of irreversible polarization through two hyperbolic tangent functions which involves AFE-FE and FE-AFE switching coercive fields. Furthermore, the piezoelectric coupling tensor is assumed to be dependent on the switching polarization, which can reflect the appearance of electromechanical coupling at the phase transition of AFE to FE. In addition, the remanent strain is assumed to be directly related to the switching polarization. Finally, the antiferroelectric-like model is implemented into FEM framework in which the nonlinear function is solved by Newton-Raphson procedure. The proposed model can capture various behaviors of both AFE and AFE-like actuators, including the 'square' double loop in pure AFE-type, slanted loop in relaxor-type and pinched-type hysteresis in which numerical results of electric displacement shows excellent agreement with measurement data. Furthermore, the induced-strain are also validated with experimental results of AFE material. The proposed method was also employed to model AFE-like actuator, in which both saturated and minor polarization and displacement hysteresis loops are captured. However, the mechanical response of AFE-like material requires further experimental investigation for validation. Moreover, although the proposed method assumes explicit expression for the irreversible polarization that might not satisfy thermodynamic law, it can act as a guidance for future work where thermodynamic consistent model will be devised.

ACKNOWLEDGMENTS

B.H. Nguyen acknowledges the Marie Skłodowska-Curie Postdoctoral Fellowship, grant agreement No.101063162.

DATA AVAILABILITY STATEMENT

The data that support the findings of this study are available from the corresponding author upon reasonable request.

□

APPENDIX

FINITE ELEMENT APPROXIMATION

In this Appendix, the stiffness matrices and force vectors in Section 3 are given in the following

$$\mathbf{K}_t^{uu} = \int_{\Omega} (\mathbf{B}^u)^T \mathbf{C} \mathbf{B}^u d\Omega, \quad (1a)$$

$$\mathbf{K}_t^{u\phi} = \int_{\Omega} (\mathbf{B}^u)^T \mathbb{E}^{\sigma} \mathbf{B}^{\phi} d\Omega, \quad (1b)$$

$$\mathbf{K}_t^{\phi u} = \int_{\Omega} (\mathbf{B}^{\phi})^T \mathbb{E}^D \mathbf{B}^u d\Omega, \quad (1c)$$

$$\mathbf{K}_t^{\phi\phi} = \int_{\Omega} (\mathbf{B}^{\phi})^T \mathbb{K} \mathbf{B}^{\phi} d\Omega, \quad (1d)$$

$$\mathbf{r}_i^u = \int_{\Omega} (\mathbf{B}^u)^T \boldsymbol{\sigma} d\Omega, \quad (1e)$$

$$\mathbf{r}_i^{\phi} = \int_{\Omega} (\mathbf{B}^{\phi})^T \mathbf{D} d\Omega, \quad (1f)$$

$$\mathbf{f}_u = \int_{\partial\Omega} (\mathbf{N}^u)^T \bar{\mathbf{t}} d\partial\Omega, \quad (1g)$$

$$\mathbf{f}_{\phi} = \int_{\partial\Omega} (\mathbf{N}^{\phi})^T \bar{\omega} d\partial\Omega, \quad (1h)$$

where the approximating matrices for the displacement and electric potential are

$$\mathbf{N}^u = [\mathbf{N}^1 \ \mathbf{N}^2 \ \dots \ \mathbf{N}^8], \quad (2a)$$

$$\mathbf{N}^{\phi} = [N_1 \ N_2 \ \dots \ N_8], \quad (2b)$$

in which $\mathbf{N}^i = \begin{bmatrix} N_i & 0 & 0 \\ 0 & N_i & 0 \\ 0 & 0 & N_i \end{bmatrix}$, with N_i are the linear shape functions of hexahedral element. Moreover, by using the kinematic relationships (3), the matrices of derivatives of shape functions \mathbf{B}^u and \mathbf{B}^φ are given as

$$\mathbf{B}^u = [\mathbf{B}^{u,1} \ \mathbf{B}^{u,2} \ \dots \ \mathbf{B}^{u,8}], \quad (3a)$$

$$\mathbf{B}^\varphi = [\mathbf{B}^{\varphi,1} \ \mathbf{B}^{\varphi,2} \ \dots \ \mathbf{B}^{\varphi,8}], \quad (3b)$$

where

$$\mathbf{B}^{u,i} = \begin{bmatrix} N_{i,x} & 0 & 0 \\ 0 & N_{i,y} & 0 \\ 0 & 0 & N_{i,z} \\ 0 & N_{i,z} & N_{i,y} \\ N_{i,z} & 0 & N_{i,x} \\ N_{i,y} & N_{i,x} & 0 \end{bmatrix}, \mathbf{B}^{\varphi,i} = \begin{bmatrix} -N_{i,x} & 0 & 0 \\ 0 & -N_{i,y} & 0 \\ 0 & 0 & -N_{i,z} \end{bmatrix}, \quad (4)$$

where $N_{i,x}, N_{i,y}, N_{i,z}$ are the spatial derivative of the shape functions with respect to x, y, z directions, respectively.

REFERENCES

1. Randall CA, Fan Z, Reaney I, Chen LQ, Trolier-McKinstry S. Antiferroelectrics: History, fundamentals, crystal chemistry, crystal structures, size effects, and applications. *Journal of the American Ceramic Society*. 2021;104(8):3775–3810.
2. Hao X, Zhai J, Kong LB, Xu Z. A comprehensive review on the progress of lead zirconate-based antiferroelectric materials. *Progress in materials science*. 2014;63:1–57.
3. Falkowski M. *Doping of HfO₂ and ZrO₂ to improve the piezoelectric properties*. PhD thesis. Technische Universität München, 2020.
4. Xu B, Pai NG, Wang QM, Cross LE. Antiferroelectric thin and thick films for high-strain microactuators. *Integrated Ferroelectrics*. 1998;22(1-4):545–557.
5. Mirshekarloo MS, Zhang L, Yao K, Sritharan T. Electromechanical properties and fatigue of antiferroelectric (Pb, La)(Zr, Sn, Ti) O₃ thin film cantilevers fabricated by micromachining. *Sensors and Actuators A: Physical*. 2012;187:127–131.
6. Bösecke T, Müller J, Bräuhäus D, Schröder U, Böttger U. Ferroelectricity in hafnium oxide thin films. *Applied Physics Letters*. 2011;99(10).
7. Müller J, Bösecke T, Bräuhäus D, et al. Ferroelectric ZrO₂. 5HfO₂. 5O₂ thin films for nonvolatile memory applications. *Applied Physics Letters*. 2011;99(11).
8. Park MH, Lee YH, Kim HJ, et al. Ferroelectricity and antiferroelectricity of doped thin HfO₂-based films. *Advanced Materials*. 2015;27(11):1811–1831.
9. Kirbach S, Lederer M, Eßlinger S, et al. Doping concentration dependent piezoelectric behavior of Si: HfO₂ thin-films. *Applied Physics Letters*. 2021;118(1).
10. Damjanovic D. Ferroelectric, dielectric and piezoelectric properties of ferroelectric thin films and ceramics. *Reports on progress in physics*. 1998;61(9):1267.
11. Mikolajick T, Slesazek S, Park MH, Schroeder U. Ferroelectric hafnium oxide for ferroelectric random-access memories and ferroelectric field-effect transistors. *Mrs Bulletin*. 2018;43(5):340–346.
12. Kirbach S, Kühnel K, Weinreich W. Piezoelectric hafnium oxide thin films for energy-harvesting applications. In: IEEE. 2018:1–4.
13. Ghatge M, Walters G, Nishida T, Tabrizian R. An ultrathin integrated nanoelectromechanical transducer based on hafnium zirconium oxide. *Nature Electronics*. 2019;2(11):506–512.
14. Hwang S, Lynch C, McMeeking R. Ferroelectric/ferroelastic interactions and a polarization switching model. *Acta metallurgica et materialia*. 1995;43(5):2073–2084.
15. Hwang SC, Huber JE, McMeeking RM, Fleck NA. The simulation of switching in polycrystalline ferroelectric ceramics. *Journal of Applied Physics*. 1998;84(3):1530–1540.
16. Hwang SC, McMeeking RM. A finite element model of ferroelectric polycrystals. *Ferroelectrics*. 1998;211(1):177–194.
17. Arockiarajan A, Menzel A, Delibas B, Seemann W. Micromechanical modeling of switching effects in piezoelectric materials—a robust coupled finite element approach. *Journal of intelligent material systems and structures*. 2007;18(9):983–999.
18. Bassiouny E, Ghaleb A, Maugin G. Thermodynamical formulation for coupled electromechanical hysteresis effects—I. Basic equations. *International Journal of Engineering Science*. 1988;26(12):1279–1295.
19. Cocks AC, McMeeking RM. A phenomenological constitutive law for the behaviour of ferroelectric ceramics. *Ferroelectrics*. 1999;228(1):219–228.
20. Kamlah M, Tsakmakis C. Phenomenological modeling of the non-linear electro-mechanical coupling in ferroelectrics. *International journal of solids and structures*. 1999;36(5):669–695.
21. Landis CM. Fully coupled, multi-axial, symmetric constitutive laws for polycrystalline ferroelectric ceramics. *Journal of the Mechanics and Physics of Solids*. 2002;50(1):127–152.
22. McMeeking RM, Landis CM. A phenomenological multi-axial constitutive law for switching in polycrystalline ferroelectric ceramics. *International Journal of Engineering Science*. 2002;40(14):1553–1577.
23. Klinkel S. A phenomenological constitutive model for ferroelastic and ferroelectric hysteresis effects in ferroelectric ceramics. *International Journal of Solids and Structures*. 2006;43(22-23):7197–7222.
24. Nguyen B, Zunic M, Torri G, Rochus V. A simple modeling of ferroelectric actuator based on phenomenological model. In: IEEE. 2023:1–5.
25. Nguyen BH, Torri GB, Zunic M, Rochus V. Simplified phenomenological model for ferroelectric micro-actuator. *Micromachines*. 2023;14(7):1355.
26. Kaltenbacher M. *Numerical simulation of mechatronic sensors and actuators*. 2. Springer, 2007.

27. Kaltenbacher M, Kaltenbacher B, Hegewald T, Lerch R. Finite element formulation for ferroelectric hysteresis of piezoelectric materials. *Journal of Intelligent Material Systems and Structures*. 2010;21(8):773–785.
28. Mayergoyz I. Mathematical models of hysteresis. *IEEE Transactions on magnetics*. 1986;22(5):603–608.
29. Butz A, Klinkel S, Wagner W. A geometrically and materially non-linear piezoelectric three-dimensional-beam finite element formulation including warping effects. *International journal for numerical methods in engineering*. 2008;76(5):601–635.
30. Schulz K, Klinkel S, Wagner W. A finite element formulation for piezoelectric shell structures considering geometrical and material non-linearities. *International journal for numerical methods in engineering*. 2011;87(6):491–520.
31. Chen W, Lynch C. A model for simulating polarization switching and AF-F phase changes in ferroelectric ceramics. *Journal of Intelligent Material Systems and Structures*. 1998;9(6):427–431.
32. Zhang J. Phase-field model simulation of ferroelectric/antiferroelectric materials microstructure evolution under multiphysics loading. 2014.
33. Saha AK. *Modeling and Applications of Ferroelectric Based Devices*. PhD thesis. Purdue University Graduate School, 2021.
34. Ali T, Lehniger D, Lederer M, et al. Tuning hybrid ferroelectric and antiferroelectric stacks for low power FeFET and FeRAM applications by using laminated HSO and HZO films. *Advanced Electronic Materials*. 2022;8(5):2100837.
35. Hegewald T, Leder E, Kaltenbacher M, Lerch R. Efficient Modeling of Ferroelectric Behavior for the Finite Element Analysis of Piezoelectric Actuators. In: IEEE. 2006:236–239.
36. Miller S, Nasby R, Schwank J, Rodgers M, Dressendorfer P. Device modeling of ferroelectric capacitors. *Journal of applied physics*. 1990;68(12):6463–6471.
37. Miller S, Schwank J, Nasby R, Rodgers M. Modeling ferroelectric capacitor switching with asymmetric nonperiodic input signals and arbitrary initial conditions. *Journal of applied physics*. 1991;70(5):2849–2860.
38. Yang J, others. *An introduction to the theory of piezoelectricity*. 9. Springer, 2005.
39. Tapily K, Jakes J, Gu D, Baumgart H, Elmustafa A. Nanomechanical study of amorphous and polycrystalline ALD HfO₂ thin films. *International Journal of Surface Science and Engineering*. 2011;5(2-3):193–204.
40. Hopcroft MA, Nix WD, Kenny TW. What is the Young's Modulus of Silicon?. *Journal of microelectromechanical systems*. 2010;19(2):229–238.
41. Dutta S, Buragohain P, Glinsek S, et al. Piezoelectricity in hafnia. *Nature Communications*. 2021;12(1):7301.
42. Liu X, Zhou D, Guan Y, Li S, Cao F, Dong X. Endurance properties of silicon-doped hafnium oxide ferroelectric and antiferroelectric-like thin films: A comparative study and prediction. *Acta Materialia*. 2018;154:190–198.